Lawrence Berkeley National Laboratory

Recent Work

Title

Hole Transfer from Photoexcited Quantum Dots: The Relationship between Driving Force and Rate

Permalink

https://escholarship.org/uc/item/7wb25285

Journal

Journal of the American Chemical Society, 137(49)

ISSN

0002-7863

Authors

Olshansky, Jacob H.
Ding, Tina X.
Lee, Youjin V.
et al.

Publication Date

2015-12-16

Hole Transfer from Photoexcited Quantum Dots: The Relationship between Driving Force and Rate

Jacob H. Olshansky,[†,⊥,§] Tina X. Ding,[†,⊥,§] Youjin V. Lee,[†] Stephen R. Leone,[†,‡,∥] and A. Paul Alivisatos[*,†,⊥,#,§]

[†]Department of Chemistry, [#]Department of Materials Science and Engineering, and [‡]Department of Physics, University of California, Berkeley, Berkeley, California 94720, United States
[⊥]Material Sciences Division and [∥]Chemical Sciences Division, Lawrence Berkeley National Laboratory, Berkeley, California 94720, United States
[§]Kavli Energy NanoScience Institute, Berkeley, California 94720, United States

Ⓢ *Supporting Information*

ABSTRACT: We have investigated the relationship between driving force and rate for interfacial hole transfer from quantum dots (QDs). This relationship is experimentally explored by using six distinct molecular hole acceptors with an 800 meV range in driving force. Specifically, we have investigated ferrocene derivatives with alkyl thiol moieties that strongly bind to the surface of cadmium chalcogenide QDs. The redox potentials of these ligands are controlled by functionalization of the cyclopentadiene rings on ferrocene

with electron withdrawing and donating substituents, thus providing an avenue for tuning the driving force for hole transfer while holding all other system parameters constant. The relative hole transfer rate constant from photoexcited CdSe/CdS core/shell QDs to tethered ferrocene derivatives is determined by measuring the photoluminescence quantum yield of these QD−molecular conjugates at varying ferrocene coverage, as determined via quantitative NMR. The resulting relationship between rate and energetic driving force for hole transfer is not well modeled by the standard two-state Marcus model, since no inverted region is observed. Alternative mechanisms for charge transfer are posited, including an Auger-assisted mechanism that provides a successful fit to the results. The observed relationship can be used to design QD−molecular systems that maximize interfacial charge transfer rates while minimizing energetic losses associated with the driving force.
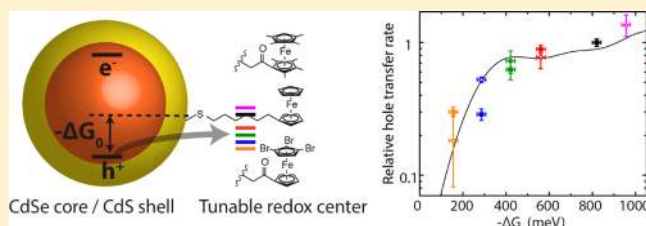
INTRODUCTION

Understanding the dynamics of charge carriers in photoexcited quantum dots (QDs) is an integral part of both designing new and refining existing QD-based technologies. These applications almost exclusively rely on efficiently harnessing the energy stored in an excited electron−hole pair either through radiative recombination or through charge separation to produce chemical or electrical work. To date, the majority of commercially viable applications rely on the former process. The sharp fluorescent linewidths, photostability, and color-tunability of QDs have led to their use in bio-imaging[1,2] and display technologies.[3] QDs have also shown great promise as potential light absorbers in photovoltaic[4−7] and photocatalytic devices[8−10] that rely on efficient charge separation.

Both fluorescence and charge transfer processes, however, must compete with deleterious recombination pathways such as charge trapping to localized interfacial and surface states. Mechanistic understanding of many of these competing de-excitation pathways, however, is still lacking owing to a difficult-to-characterize spatial separation and energetic distribution of contributing states. In this study, we aim to improve our understanding of one of these pathways by studying hole

transfer in a model system containing well-defined donor−acceptor separation and energetic ordering. This could inform the design of brighter QDs for displays and bio-imaging since hole transfer to trap states is a common cause of nonunity photoluminescence quantum yields.[11−13] Alternatively, a deeper understanding of interfacial hole transfer could greatly improve the design of QD-based solar conversion schemes since hole transfer has been shown to be a major factor limiting efficiencies in colloidal hydrogen generation schemes[14] as well as QD-sensitized solar cells.[15,16]

These applications would not only benefit from a mechanistic understanding of hole transfer, but also from an empirical relationship between the thermodynamic driving force for charge transfer and the associated rate of hole transfer. The efficiency of a device will ultimately be dictated by both these quantities. The driving force for initial charge separation will necessarily reduce the potential energy output of the device, resulting in reductions in either the open circuit voltage (photovoltaics) or in the achievable chemical work (photo-
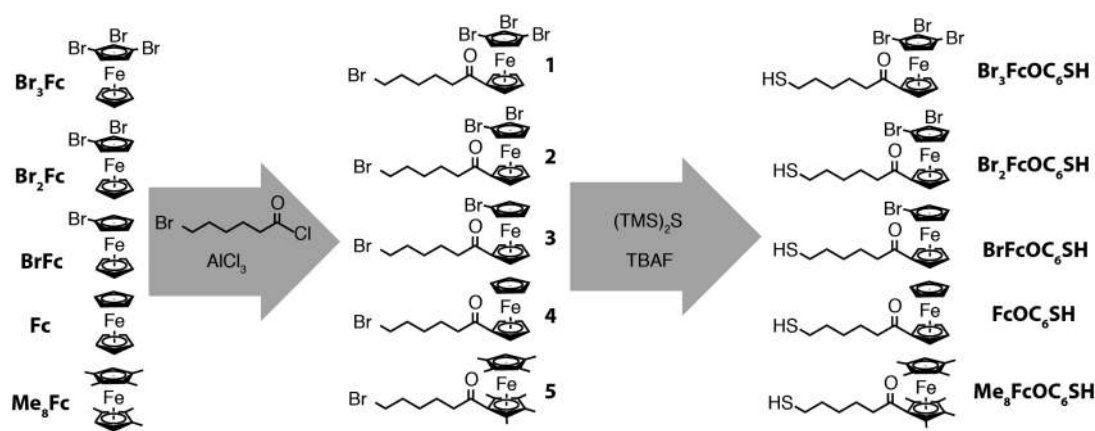
Figure 1. Scheme for synthesis of Br$_3$FcOC$_6$SH, Br$_2$FcOC$_6$SH, BrFcOC$_6$SH, FcOC$_6$SH, and Me$_8$FcOC$_6$SH via a Friedel−Crafts acylation to make compounds **1**−**5**, followed by a thiolation reaction with bis(trimethylsilyl)sulfide to produce the desired products (see Supporting Information for further detail).

catalysis). Similarly, the rate for charge transfer will affect quantities such as the short circuit current (photovoltaics) and quantum efficiency (photocatalysis). Generally, one would want to maximize the rate while minimizing the potential energy loss associated with the driving force. To date, a clear relationship between the rate for hole transfer from photoexcited QDs and the driving force has not yet been reported and is the aim of the present work.

The relationship between driving force and rate between molecular species has been well described by Marcus theory,[17] which predicts the rate to initially increase with driving force within the normal regime and then to decrease with further increases in driving force, defining the inverted regime. The existence of these two regimes has been shown to be crucial for efficient energy conversion present in photosynthetic centers.[17] Although Marcus theory is certainly applicable to QD systems, many specifics of its implementation are not well established. Energy conversion applications using QD-based systems would therefore benefit from a robust model for charge transfer and has motivated a considerable body of work on both electron[18−24] and hole transfer[25−30] from QDs to acceptor molecules in the past decade. However, clear relationships between driving force and rate have been difficult to chart due to inherent heterogeneities in ensembles of QD−molecular conjugates, a limited set of tools for accurately probing the QD surface, and a lack of control in varying the driving force without also affecting other key parameters.[31] Many QD−molecular charge transfer studies employ molecular species that weakly bind to the QD surface in an ill-defined manner, thus eliminating the ability to accurately determine a reliable charge transfer rate per molecule. A recent review by Knowles et al.[31] highlights much of this work and the associated difficulties in performing mechanistic studies on QD−molecular charge transfer systems.

Nevertheless, a handful of systematic studies on QDs relating *electron* transfer rates to driving force have been reported, all of which observe Marcus behavior in the normal regime.[18,19,23] The groups of Lian and Prezhdo recently published a comprehensive experimental study mapping the relationship for the electron transfer rate as a function of driving force using CdTe, CdSe, and CdS QDs of varying size coupled with three distinct molecular acceptors, covering a larger range in driving force than has previously been probed.[23] The primary mode for controlling driving force in many of these studies relies on

changing the QD size and thus also the conduction band energy. However, this makes it difficult to control the changes in electronic coupling, since one would expect smaller QDs to be more efficiently coupled to surface bound acceptors. The work from the groups of Lian and Prezhdo accounted for this variation with an effective mass model that normalized the electronic coupling factor to electron density on the surface of the QD.[23]

This work showed no inverted regime for electron transfer, with the charge transfer rate constant saturating at the highest driving forces. Lian and Prezhdo postulated that as the electron transfers to the molecular acceptor the lost energy is coupled to the excitation of the residual hole in the valence band, similar to the Auger effect responsible for nonradiative recombination in systems with an extra charge. Electron transfer coupled with hole excitation allows the rate to stay high at large driving force since there are many potential final states associated with hole excitation, one of which will have a driving force near the barrierless region. They found that their data fits well to this proposed model.

The analogous hole transfer, however, may deviate from this behavior for a few reasons. First, the electron density of states is significantly lower than the hole density of states in cadmium chalcogenide QDs. Although it should be noted that according to the Auger-assisted model, the electron density of states for our system is still large enough to eliminate any inverted region dynamics at room temperature. Second, since there is still no spectroscopic evidence for core charge excitation during charge transfer, another possibility is that the Auger-assisted model is operating via excitation of trapped charges. Therefore, the differing trap state densities of electrons and holes would affect the results. Finally, the electronic coupling between initial and final states in the Auger-assisted model will certainly change for hole transfer coupled with electron excitation. We seek to experimentally determine the existence of this Auger-assisted behavior for hole transfer. To do this, we constructed a model system for systemically mapping the rate constant of hole transfer as a function of driving force.

In this experimental model system, we use QDs with quantum yield exceeding 80% in order to suppress native nonradiative charge transfer pathways. We covalently attach ferrocene hole acceptors onto the QD surface and quantitatively measure the ferrocene surface coverage via NMR. We have previously demonstrated the effectiveness of this model to
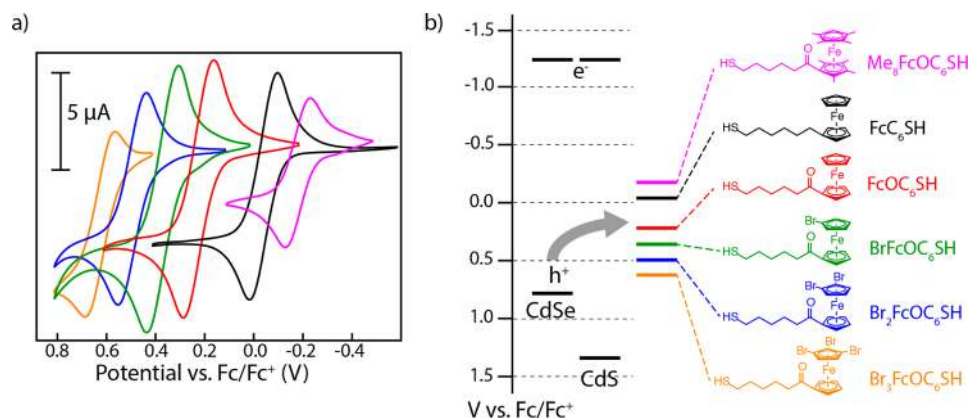
Figure 2. Energy diagram. (a) Cyclic voltammograms of the ferrocene ligands collected in 0.1 M TBA-PF$_6$ in THF, scanned at 10 mV s^{-1} and referenced to Fc/Fc$^+$. Br$_3$FcOC$_6$SH (orange), Br$_2$FcOC$_6$SH (blue), BrFcOC$_6$SH (green), FcOC$_6$SH (red), FcC$_6$SH (black), and Me$_8$FcOC$_6$SH (magenta). (b) Energy diagram of CdSe and CdS valence and conduction bands relative to the six ferrocene ligands used in the study.

measure hole transfer rate constants per acceptor for nine different systems spanning a large range in electronic coupling. In this previous work, photoluminescence quantum yield and time-resolved fluorescence spectroscopy were used to extract the rate constant per acceptor for each system.[30] This current work utilizes the previous methodologies to further enhance our understanding of QD charge transfer by examining the relationship of the rate constant to the thermodynamic driving force. To achieve modulation in driving force, we synthetically functionalize the cyclopentadiene ring of ferrocene with electron withdrawing and donating groups to tune the oxidation potential of the molecule by approximately 800 meV, spanning a driving force range of 150–950 meV. Again, the well-defined nature of our donor−acceptor system enables us to vary driving force without significantly changing other parameters of the system that may affect the rate constant. Specifically, we hold the size of the QD core, the linker length, and the headgroup of the ligand of our system constant. The present work demonstrates the first systematic study of the relationship between rate and driving force for hole transfer from photoexcited QDs.

RESULTS AND DISCUSSION

Hole Acceptors with Systematically Variable Driving Force. Five ferrocene derivatives with oxidation potentials spanning 800 meV in energy were synthesized (Figure 1). The redox potentials were controlled by modification of the cyclopentadienyl rings with either electron donating or withdrawing groups. In this study, the electron-withdrawing group was bromine, which was found to lower the energy of the highest occupied molecular orbital (HOMO) on ferrocene by approximately 130 meV per additional bromine, in accordance with previous literature results.[32] To achieve higher HOMO energies, electron donating methyl substituents were employed. Higher HOMO energies will correspond to larger driving forces for hole transfer from the QD to the ferrocene. All the ligands were synthesized with a six-carbon linker and a thiol binding head to covalently attach to the surface of the QD. Five ligands were synthesized starting with either 1,2,3-tribromoferrocene (Br$_3$Fc), 1,2-dibromoferrocene (Br$_2$Fc), bromoferrocene (BrFc), ferrocene (Fc), or bis(tetramethylcyclopentadienyl)-iron (Me$_8$Fc). Of these, BrFc, Fc, and Me$_8$Fc were available commercially, while Br$_2$Fc and Br$_3$Fc were synthesized from BrFc.

The linker group and binding head were added to Br$_3$Fc, Br$_2$Fc, BrFc, Fc, and Me$_8$Fc via a Friedel−Crafts acylation with 6-bromohexanoyl chloride followed by a thiolation[33] (Figure 1). As expected, owing to the electron-withdrawing nature of bromine, the acylation occurred on the cyclopentadienyl ring that had not been brominated in the cases of BrFc, Br$_2$Fc, and Br$_3$Fc. This observation was confirmed by ^{1}H NMR. It should also be noted that the Me$_8$Fc synthesis suffered from a particularly low yield due to its propensity to oxidize under the conditions required for a Friedel−Crafts acylation (see Supporting Information).[34] A sixth ligand, 6-ferrocenylhexane-thiol (FcC$_6$SH), available commercially, was also used in this study.

Cyclic voltammetry was used to determine the reversible potentials, and thus HOMO energies of the ferrocene derived ligands. The ligands were referenced to unfunctionalized ferrocene and cover an 800 meV range in potentials (Figure 2a). It should be noted that the electrochemistry on the ferrocene derivatives was performed in the reductively stable electrochemical solvent of tetrahydrofuran, while the optical studies to determine charge transfer rates were performed in chloroform-d diluted into chloroform, to allow for direct optical measurement of the NMR solutions. This may lead to a slight systematic deviation in the precise value of the driving force, yet the range and the trend will remain the same. We believe that this deviation will be ∼10% since the difference in measured redox potentials between ferrocene and decamethylferrocene is 483 mV in chloroform and 427 mV in tetrahydrofuran.[35]

The band energies of the CdSe/CdS core/shell QDs were also referenced to ferrocene via low temperature cyclic voltammetry measurements of the conduction band edge, which was observed at −1.25 (±0.05) V vs ferrocene (see Supporting Information). This measurement probes the lowest energy electronic state, which for CdSe/CdS core/shell systems has been shown to be delocalized over both the core and the shell.[36−38] Therefore, this state is electrochemically accessible and its measurement gives us the LUMO energy of the core/shell system. The QDs used for this measurement had a fluorescence peak at 2.03 eV. Assuming this to be the difference in energy between the conduction band of the core/shell system and the valence band of CdSe, we determined its valence band energy to be approximately +0.78 (±0.05) V vs ferrocene (Figure 2b). This value is in good agreement with our previous study on CdSe/CdS core/shell rods that employed
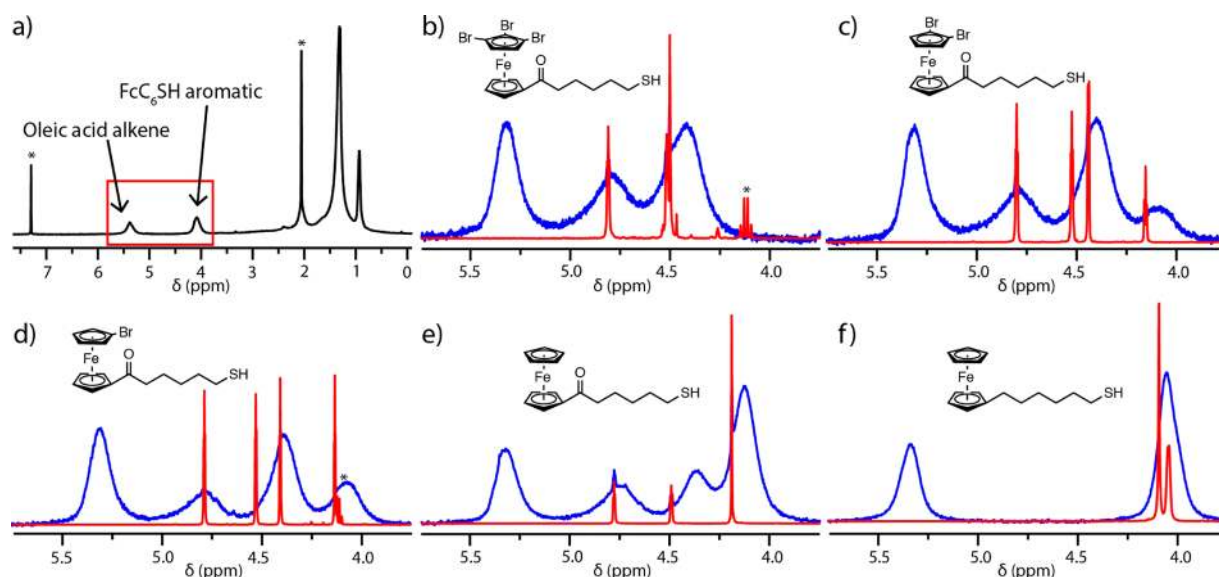
Figure 3. ^{1}H NMR spectra of ferrocene ligands. (a) Full spectrum of a QD sample with partial ligand exchange from the native oleate ligand to FcC$_6$SH. Solvent peaks (denoted by *) are from chloroform, acetonitrile, and ethyl acetate. (b−f) Expanded spectra on the ppm region of interest, which includes ferrocene aromatic protons and oleic acid alkene protons. (Red) spectra of ferrocene ligands free in solution, and (blue) spectra of ligands bound to QD surface, including oleate.

the same experimental technique corroborated by theoretical work to determine the position of the valence band edge of the CdSe core at +0.8 V vs ferrocene.[29] Slight deviations may be a result of the smaller CdSe cores used in the rod study, which would shift the valence band down by a small amount.

Relative Rate Constants of Hole Transfer. With a well-characterized and sizable range in driving forces established, we prepared QD−molecular conjugates and measured relative charge transfer rate constants by monitoring the photoluminescence quenching as a function of ferrocene coverage. Our previous work has shown that this quenching is directly attributed to hole transfer to ferrocene, scaling accordingly to coverage and coupling.[30] To accurately determine the relative ligand coverage per QD, we turned to quantitative ^{1}H NMR. This technique has risen in popularity in recent years since it can be used to accurately determine the concentration of surface bound species. Furthermore, surface bound species exhibit dramatically broadened peaks with widths of 50−100 Hz.[30,39−41] This makes them easy to distinguish from species free in solution, however, the broadening complicates one's ability to accurately quantify the bound peaks. Any protons in the crowded methyl and methylene regions shifted by 1−3.5 ppm are often too convoluted for accurate quantification. Typically, resonances downfield from 4 ppm are easier to quantify such as the protons on the alkene of oleic acid at 5.3 ppm.[40,41]

The current work quantifies ligand coverage by integration of the aromatic protons on the ferrocene derivatives (4−5 ppm) and referencing to an external standard. Since, the native ligands are primarily oleic acid with some residual octadecylphosphonic acid (ODPA), only the ferrocene resonances appear within the 4−5 ppm range (see Figure 3). This allows for accurate quantification of the concentration of all surface bound acceptor molecules in this study except for Me$_8$FcOC$_6$SH. This particular derivative has only one aromatic proton at 3.33 ppm, thus making it difficult to directly quantify. We therefore monitored loss of oleic acid as a proxy for Me$_8$FcOC$_6$SH coverage. In all other ligand exchanges, and in

our previous work,[30] we observed an approximate 1:1 exchange between the ferrocene thiol ligand and oleic acid, with deviations on the order of 10−15% (see Supporting Information). We therefore are confident that this method is accurate, yet prone to slightly larger uncertainty than direct quantification.

To determine the relative rate constants for hole transfer among these ferrocene derivatives, we measured the photoluminescence quantum yield (PLQY) with varying surface concentrations of the acceptor ligand. If the radiative rate constant (k_r) and native-nonradiative rate constant (k_{nr}) of a QD sample are known, a plot of PLQY vs N (average number of acceptor molecules per QD) will yield a unique hole transfer rate constant per ligand (k_{ht}) (eq 1). It should be noted that this analysis relies on the fact that k_r and k_{nr} remain constant for a given QD as N is increased. Our previous work with similar QD samples and analogous ferrocene ligands found this assumption to be valid with multiple shell thicknesses and linker lengths. All of these QD−molecular conjugates exhibited behavior well modeled by eq 1 and yielded values for k_{ht} consistent with tunneling through the shell and organic linker, while the thiol binding head was found to have a negligible effect on the quenching. Additionally, we showed that we are operating in a large N regime in which an average N is a fine approximation for describing the distribution of ligands on QDs. Using the more physically accurate Poisson distribution of bound ligands has a minimal impact on the results.[30]

Equation 1 can be reformulated in terms of the native PLQY (QY$_0$), a relative ferrocene concentration (rel. Fc conc.), and a coefficient, a, proportional to k_{ht}. The rel. Fc conc. is the ratio of surface-bound ferrocene concentration (in mM) measured via NMR to the optical extinction of QDs at 500 nm in the same solution (eq 2). Therefore, the relative ferrocene concentration serves as a proxy for the number of acceptor molecules per QD and will be proportional to N for a given batch of QDs. The a factor can then be related to a ratio of de-excitation rate constants as well as the molar extinction coefficient for the QDs at 500 nm (ε_{500nm}) (eq 3).

$$PLQY = \frac{k_r}{k_r + k_{nr} + Nk_{ht}} = \frac{QY_0}{1 + (\text{rel. Fc conc.})a} \quad (1)$$

$$\text{rel. Fc conc.} = \frac{[\text{Fc ligand}]}{QD\ Abs_{500nm}} \quad (2)$$

$$a = \varepsilon_{500nm}\frac{k_{ht}}{k_r + k_{nr}} = bk_{ht} \quad (3)$$

While there have been extensive studies on determining the extinction coefficient for single composition QDs,[42,43] it is difficult to accurately determine extinction coefficients for core/shell QDs. Since we were primarily interested in relative rates for charge transfer between ligands, it sufficed to leave ε_{500nm} as an unknown constant, and perform our analysis based on the fact that a would be proportional to k_{ht}, related by a constant, b, that will be invariant for a given batch of QDs. An example PLQY vs rel. Fc conc. plot is shown in Figure 4 for one batch of
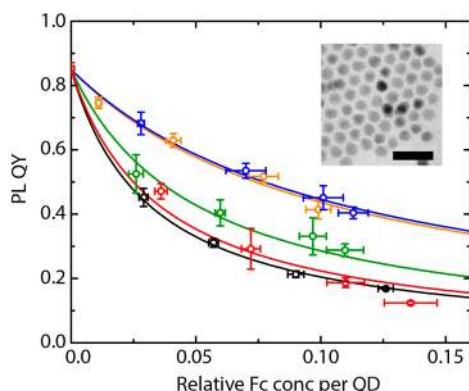

Figure 4. Photoluminescence quantum yield (PLQY) of QD sample 1 as a function of the relative concentration of ferrocene ligand bound to the surface. Fits to eq 1 are shown as solid lines. Br$_3$FcOC$_6$SH (orange), Br$_2$FcOC$_6$SH (blue), BrFcOC$_6$SH (green), FcOC$_6$SH (red), and FcC$_6$SH (black) were exchanged onto this sample. Inset: TEM micrograph of QD sample 1 with 25 nm scale bar.

QDs, of which five portions underwent ligand exchange with five of the ferrocene derivatives used in this study. PLQY vs relative ferrocene concentration relationships were constructed by performing successive ligand exchange reactions on portions of QD stock solutions containing approximately 10−25 μmol of surface-bound oleate ligand in 0.6 mL of solution. Lower concentrations resulted in NMR spectra that were too noisy to easily interpret, while higher concentrations consumed too many QDs. Owing to difficulty in scaling up the core synthesis and the subsequent shelling reaction, the quantity of QDs in a given batch limited our ability to perform all ligand exchanges on a single sample of QDs. Therefore, ligand exchanges were performed on five separate batches of QDs with similar valence band positions, ensuring consistent driving forces. Since the CdSe core dictates the valence band position, similar sized cores were used in all core/shell syntheses. The cores used had first absorption peaks of 563, 565, 560, 560, and 559 nm, which would result in deviations in the valence band of no more than 10 meV.

The five QD samples did vary significantly in CdS shell thickness, with total diameters ranging from 7.3 to 11.9 nm. The data shown in Figure 4 are from the 7.3 nm sample (QD sample 1), which was synthesized on a large enough scale to enable five ligand exchanges. PLQY vs rel. Fc conc. for the four other QD samples (samples 2−5) are available in the Supporting Information. Although the values of k_{ht} will certainly vary with shell thickness for a given ligand as the electronic coupling between donor and acceptor will change dramatically, our past work has shown that the ratio of hole transfer rate constants for two distinct ligands is consistent across multiple shell thicknesses.[30] We therefore report a relative hole transfer rate constant (relative k_{ht}) for each ligand by referencing to the quenching rate of FcC$_6$SH, which was exchanged onto QD samples 1−5. This relative hole transfer rate constant is the ratio of the a value for a given ligand on QD sample x to the a value for FcC$_6$SH on QD sample x.

Driving Force versus Rate Constant Relationship. Scaling the relative hole transfer rate constants on each QD to the value measured for FcC$_6$SH allows us to represent all collected data on one plot of relative k_{ht} vs driving force (Figure 5). Uncertainties were generated from bootstrap error analysis
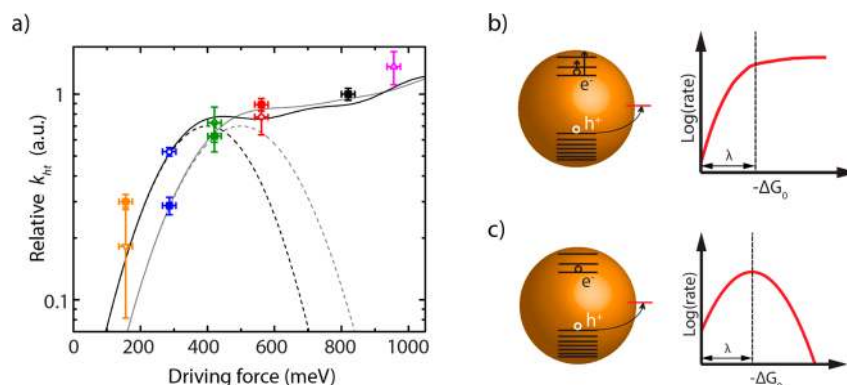
Figure 5. Driving force vs rate constant. (a) Plot of the relative hole transfer rate constant as a function of driving force. Data for ferrocene ligands collected on different QD samples are scaled to the rate constant for FcC$_6$SH (set to one). Filled square data points are from QD sample 1, all unfilled data points are from QD samples 2−5. The dashed lines show behavior expected from a two-state Marcus model (eq 4). The solid lines show behavior expected from the Auger-assisted model (eq 5). Reorganization energies of (black) 400 and (gray) 500 meV were used. (b) Schematic of general behavior predicted by the Auger-assisted model for charge transfer. The electronic excitation in the conduction band occurs during hole transfer, thus reducing the effective driving force and eliminating the inverted region. (c) Schematic of behavior predicted by the two-state Marcus model. Without the coupled electronic excitation, one would expect an inverted region.

while fitting the PLQY vs rel. Fc conc. data, incorporating the experimental error present in both the PLQY and rel. Fc conc. data. The errors in values of the relative k_{ht} are therefore a convolution of fitting error and experimental error. Error bars for QD samples 2−5 were constructed from both the uncertainty in relative k_{ht} for the ligand in question as well as the reference ligand, FcC$_6$SH. Since five ligands were exchanged onto QD sample 1, we have shown uncertainties for each of the ligand's relative k_{ht} values independently, including FcC$_6$SH. Each ligand, except for Me$_8$FcOC$_6$SH, was exchanged onto more than one QD sample. Therefore, the plot for driving force vs rate gives a sense of the range in relative rate constants that can be measured.

The plot of relative rate constant vs driving force was first examined in reference to the two-state nonadiabatic Marcus model (eq 4). In this model, the rate constant (k_{ct}) is expected to first increase with increasing driving force ($-\Delta G_0$), but to then decrease for driving forces greater than the reorganization energy (λ). The rate is also expected to be modulated by the electronic coupling factor ($|H_{a,b}|^2$) between the initial and final states.

$$k_{ct} = \frac{2\pi}{\hbar} |H_{a,b}|^2 \frac{1}{\sqrt{4\pi\lambda k_b T}} \exp\left(-\frac{(\lambda + \Delta G_0)^2}{4\lambda k_b T}\right) \quad (4)$$

We have simulated these Marcus parameters in our previous work on a similar system with FcC$_6$SH tethered to a CdSe/CdS nanorod.[29] In this work, density functional theory was used to determine molecular reorganization energies, while solvent reorganization was computed with a dielectric continuum model. The resultant net reorganization energy for hole transfer to FcC$_6$SH in chloroform was calculated to be approximately 500 meV. However, in the experimental system, the ferrocene ligand will also be surrounded by lower dielectric alkane ligands along with chloroform, thus reducing the reorganization energy.[29] We therefore used values for λ of 400 and 500 meV to generate expected rate vs driving force plots (Figure 5), against which we can compare our experimental data. It is clear that the standard two-state Marcus model does not fit our current data since we do not observe an inverted region. It is unlikely that this discrepancy is due to an inaccurate reorganization energy, since λ would have to be greater than 1 eV to fit our data. In water, the reorganization energy of analogous ferrocene ligands is at most 0.85 eV.[44] In the lower dielectric solvent of chloroform, this value would be decreased, and the QD would be expected to have only a minor contribution to λ.

Since there is no observable inverted region in our results, we turn to the recently posited Auger-assisted model for electron transfer from photoexcited QDs to better model our data.[23,45] In this model, charge transfer can be coupled with intraband excitation of the residual charge in the QD. This allows the rate to stay high at large driving force, since the excess energy that would go to vibrations in the standard Marcus model is instead efficiently coupled into electronic excitation (Figure 5b). The resultant rate can then be written as a sum of rates associated with each accessible electronic excitation (eq 5). For hole transfer, the values of $E_{e,i}$ correspond to conduction band energy levels relative to the band edge where $E_{e,0} = 0$.

$$k_{ct} = \sum_{i=0} \frac{2\pi}{\hbar} |H_{a,b}(E_{e,i})|^2 \frac{1}{\sqrt{4\pi\lambda k_b T}} \exp\left(-\frac{(\lambda + \Delta G_0 + E_{e,i})^2}{4\lambda k_b T}\right) \quad (5)$$

To approximate the conduction band energy levels, we used previously computed values for CdSe core QDs with band gaps equal to the band gaps of the core/shell QDs used in our study ($\sim$2 eV).[46] This corresponds to CdSe core QDs with radii of 2.8 nm and 1P$_e$, 1D$_e$ and 2S$_e$ energy levels of 315, 600, and 760 meV above the band edge. These values were used for $E_{e,i}$ in the functions plotted in Figure 5a. We also assumed that the electronic coupling does not depend on the level of electron excitation, in accordance with previous work.[23,45] It should be noted that many different conduction band energy spacings will reproduce the data we observe as long as the spacings are less than or on the order of the width of the Marcus curve $(2\lambda k_b T)^{1/2}$, which is 160 meV with λ = 500 meV at room temperature. Our estimated conduction band energy levels may underestimate the true density of states in the larger core/shell structures, but this would not change the shape of the curve significantly. For example, a linearly increasing density of states was used by Lian and Prezhdo, and this resulted in curves exhibiting similar behavior.[23] See Supporting Information for additional functional models based on eq 5 with different values of $E_{e,i}$. Despite the success of the Auger-assisted model in reproducing the experimental data, there is currently no direct spectroscopic evidence for the intraband transition associated with the Auger-assisted mechanism, and other mechanisms could be proposed. For example, Auger-assisted electronic transitions within the distribution of surface states could also be coupled to charge transfer, which would also eliminate the inverted region. Further transient spectroscopic studies that can directly probe the absorption of the coupled transition would be necessary to definitively determine which state is coupled to charge transfer.

Nevertheless, the experimental trend informs avenues for designing more efficient QD-based photoconversion devices. The results suggest that the initial hole transfer process should be driven by approximately 300−500 meV ($\sim\lambda$), but any additional driving force will result in minimal gains in rate. The results from this model system can also help to understand how charge trapping competes with QD luminescence, relevant for applications in QD emission. Specifically, because charge transfer rates to traps will not decrease at high driving force, QD trap states deep within the band gap would continue to be efficient quenchers of emission. Lastly, in the context of the Auger-assisted model, one would expect the Marcus inverted region to be present for hole transfer in charge separation systems in which the electron transfer occurs on faster time scales than hole transfer. In this case, hole transfer would occur with no electron in the conduction band, thus eliminating the possibility for Auger-assisted electron excitation. However, further work is needed to better resolve the underlying mechanism in order to confirm this predicted behavior.

■ CONCLUSIONS

We have used a well-controlled model system to determine the relationship between driving force and rate for hole transfer from photoexcited QDs. Six distinct ferrocene-derived molecular charge acceptors were used in the study, and

photoluminescence quenching was used to determine relative hole transfer rate constants. We do not observe the Marcus inverted region at high driving force, indicating that another mechanism may be needed to explain the results. We have interpreted these data in the context of the Auger-assisted mechanism for charge transfer, first proposed by Lian and Prezhdo. However, direct spectroscopic evidence for this mechanism is still lacking, leaving the possibility for other potential modes of charge transfer. The measured relationship can be used to inform the design of QD-based photoconversion devices that would aim to maximize interfacial hole transfer rates while minimizing energetic losses associated with the driving force.

■ EXPERIMENTAL METHODS

Chemicals. 6-(Ferrocenyl)hexanethiol (FcC6SH), bromoferrocene (BrFc), n-butyllithium solution (n-BuLi, 1.6 M in hexanes), 2,2,6,6-tetramethylpiperidine (TMP, ≥99.0%), zinc chloride solution (ZnCl$_2$, 1.9 M in 2-methyltetrahydrofuran), 1,1,2,2-tetrabromoethane (TBE, 98%), bromine (Br$_2$, ≥99.5%), iron(III) chloride (FeCl$_3$, 97%), ferrocene (Fc, 98%, sublimed), 6-bromohexanoyl chloride (97%), aluminum chloride (AlCl$_3$, ≥99.0%), tetrabutylammonium fluoride solution (TBAF, 1.0 M in tetrahydrofuran), trioctylphosphine oxide (TOPO, 99%), selenium (Se, 99.99%), cadmium oxide (CdO, ≥99.99%), oleic acid (OA, 90%), 1-octadecene (ODE, 90%), oleylamine (OLAM, 70%), 1-octanethiol (OctSH, ≥98.5%), chloroform-d (CDCl$_3$, 99.8 atom % D), tetrabutylammonium hexafluorophosphate (TBA-PF$_6$, ≥99.0%) and silver nitrate (AgNO$_3$, 99.9999%) were purchased from Sigma-Aldrich and used as received. Bis(tetramethylcyclopentadienyl)iron (Me$_8$Fc, 98%), tri-n-octylphosphine (TOP, 99%), and bis(pentamethylcyclopentadienyl)iron (Fc*, 99%) were purchased from STREM. Other chemicals used include octadecylphosphonic acid (ODPA, 99%, PCI Synthesis), bis-(trimethylsilyl)sulfide ((TMS)$_2$S, TCI America), silica gel (SiliaFlash P60, 40−63 μm, Silicycle), magnesium sulfate (MgSO$_4$, EMD), sodium chloride (NaCl, EMD), sodium bicarbonate (NaHCO$_3$, EMD), and the anhydrous solvents chloroform, acetone, tetrahydrofuran (THF), hexanes, dichloromethane (DCM), ethyl acetate, and acetonitrile.

Synthesis of Ferrocene Ligands. *1,2-Dibromoferrocene (Br$_2$Fc) and 1,2,3-Tribromoferrocene (Br$_3$Fc).* To achieve high specificity toward the desired products, an ortho-lithiation with lithium tetramethylpiperidide was performed on either BrFc or Br$_2$Fc followed by a transmetalation with ZnCl$_2$ to produce the less reactive aryl-zinc species prior to bromination with either Br$_2$ or TBE, thus preventing overbromination. This strategy allowed for controlled successive ortho-additions of bromine (Supporting Information, Figure S1).[47,48] Br$_3$Fc was synthesized from Br$_2$Fc with a high enough yield that a simple column and recrystallization resulted in pure Br$_3$Fc. However, bromination of BrFc to make Br$_2$Fc had a much lower yield, resulting in a 60:40 ratio of Br$_2$Fc to BrFc. Since many of the standard purification methods fail to separate halogenated ferrocenes, an electrochemical technique was employed.[49] Iron(III) chloride has a redox potential between Br$_2$Fc and BrFc, so exposure of a mixture of BrFc and Br$_2$Fc in an organic solvent to aqueous FeCl$_3$ preferentially oxidizes BrFc, thus transferring it to the aqueous phase as BrFc$^+$. Repeating this purification process multiple times resulted in pure Br$_2$Fc in the organic phase. Experimental details may be found in the Supporting Information.

Friedel−Crafts Acylation: Compounds 1−5. All compounds were synthesized in a similar manner.[33] The ferrocene derivative (Br$_3$Fc, Br$_2$Fc, BrFc, Fc, or Me$_8$Fc) and 6-bromohexanoyl chloride were dissolved in DCM. AlCl$_3$ was added at 0 °C under argon and the reaction was allowed to proceed for between 30 min and 1.5 h. The reaction was quenched with water, washed with sat. aq. NaHCO$_3$ and sat. aq. NaCl, dried over MgSO$_4$, and the solvent was removed in vacuum. The product was purified via column chromatography with

hexanes and ethyl acetate. Ratios of reactants varied between reactions. Further details may be found in the Supporting Information.

Thiolation: Br$_3$FcOC$_6$SH, Br$_2$FcOC$_6$SH, BrFcOC$_6$SH, FcOC$_6$SH, and Me$_8$FcOC$_6$SH. All thiolation reactions were performed following the same procedure.[33] In a typical reaction, the product from the Friedel−Crafts acylation was combined with (TMS)$_2$S in a vial containing 1−2 mL of THF per 100 mg of reactant. TBAF solution was then added dropwise at 0 °C under argon and the reaction was allowed to proceed for between 45 min and 1.5 h. The reaction was quenched by pouring it into cold water, diluted with diethyl ether, washed three times with water, and dried over MgSO$_4$. The solvent was removed in vacuum yielding an orange oil. Column purification was performed if necessary to remove the disulfide product.

Electrochemistry. Cyclic voltammograms (CVs) of ferrocene ligands were recorded on a CHI-600C electrochemical analyzer. Measurements were performed under argon in quiescent THF electrolyte with 0.1 M TBA-PF$_6$ as the supporting electrolyte. A freshly polished 3.0 mm diameter glassy carbon button electrode served as the working electrode and a platinum mesh served as the counter electrode. An encased silver wire electrode with a porous Teflon tip filled with a 10 mM AgNO$_3$, 0.1 M TBA-PF$_6$, acetonitrile solution served as the reference electrode (part no. CHI112, CH Instruments). The concentration of ferrocene ligand in solution was approximately 1 mM. CV scans were performed at 10, 50, 100, 250, 500, and 1000 mV s^{-1}, and $E_{1/2}$, taken at the average of the oxidation and reduction peak potentials, did not depend on scan rate. All potentials were calibrated using an Fc* ($E_{1/2}$ = −427 mV vs Fc/Fc$^+$ in THF)[35] internal standard added to the electrochemical cell after CVs were performed on the analyte.

Synthesis of CdSe/CdS Core/Shell QDs. QDs were synthesized following previously published procedures.[30,50] Multiple reactions were run under slightly varying conditions. The quantity of CdSe QDs used ranged from 250 to 900 nmols, as determined by optical extinction of the first excitonic feature.[43] In a typical reaction, CdSe QDs were first degassed at room temperature for an hour and next at 120 °C for 30 min in a solution with equal volumes of OLAM and ODE. The total volume of OLAM and ODE ranged from 3 to 6 mL per 100 nmol of QDs used. The reaction was then heated under argon to 310 °C, and held there for the duration of the shell growth. Slow injection of 0.2 M OctSH in ODE and 0.2 M cadmium oleate in ODE was started at 250 °C, and continued for 2 h. Injection solution volumes varied between 6 and 12 mL for each precursor. Upon injection completion, the reaction was maintained at 310 °C for 10 min, then cooled to room temperature. The core/shell QDs were isolated from excess ligand via precipitation in acetone and redispersion in hexanes, repeated two or three times. Insoluble impurities were often precipitated out via centrifugation in hexanes only. QDs were stored in either hexanes or chloroform in an inert environment. Experimental details for QD samples 1−5 may be found in the Supporting Information.

Ligand Exchange with CdSe/CdS Core/Shell QDs. The ligand exchange procedure is described in our previous work.[30] Ferrocene ligands were added to QD solutions at room temperature in chloroform. Since the thiol readily displaces the native oleate ligand, extent of exchange was controlled by amount of ferrocene added. Excess ligand was removed via precipitation with acetonitrile and disposal of the supernatant. The lack of significant free peaks in the ^{1}H NMR (Figure 3) indicates that this purification was successful, although incomplete cleaning sometimes resulted in free ligand at concentrations up to 5% that of the bound concentration. This could easily be quantified by peak fitting, and accounted for in determining the bound ferrocene concentration.

Quantitative NMR. Quantitative ^{1}H NMR spectra were obtained on a Bruker 400 MHz instrument. Ligand concentrations were computed from absolute integration values divided by the number of scans and referenced to a standard sample of known concentration. The standard sample was 10 mM Fc in toluene-d_8. For all quantitative NMR spectra, the 90° pulse was calibrated and the dwell time between successive scans was ensured to be at least five times T$_1$.[51]

Optical Spectroscopy. All optical measurements were performed on particles dispersed in chloroform. Absorption spectra were collected on a Shimadzu 3600 spectrophotometer with 1 nm increments. Photoluminescence emission spectra were collected on a Horiba Jobin Yvon TRIAX 320 Fluorolog. Quantum yield measurements were performed by referencing to Rhodamine 6G, see Supporting Information for details.[52]

■ ASSOCIATED CONTENT

Ⓢ Supporting Information

The Supporting Information is available free of charge on the ACS Publications website at DOI: 10.1021/jacs.5b10856.

> Details of the synthesis of ferrocene ligands and QDs; electrochemical measurement of QD conduction band; additional PLQY quenching data and details of the ligand exchanges; fluorescence QY determination; additional fits to the data using the Auger-assisted model; instrumentation (PDF)

■ AUTHOR INFORMATION

Corresponding Author

*apalivisatos@lbl.gov

Notes

The authors declare no competing financial interest.

■ ACKNOWLEDGMENTS

■ REFERENCES

(1) Medintz, I. L.; Uyeda, H. T.; Goldman, E. R.; Mattoussi, H. *Nat. Mater.* **2005**, *4*, 435−446.

(2) Pinaud, F.; Michalet, X.; Bentolila, L. A.; Tsay, J. M.; Doose, S.; Li, J. J.; Iyer, G.; Weiss, S. *Biomaterials* **2006**, *27*, 1679−1687.

(3) Shirasaki, Y.; Supran, G. J.; Bawendi, M. G.; Bulović, V. *Nat. Photonics* **2013**, *7*, 13−23.

(4) Kramer, I. J.; Sargent, E. H. *Chem. Rev.* **2014**, *114*, 863−882.

(5) Chuang, C.-H. M.; Brown, P. R.; Bulović, V.; Bawendi, M. G. *Nat. Mater.* **2014**, *13*, 796−801.

(6) Kamat, P. V. *Acc. Chem. Res.* **2012**, *45*, 1906−1915.

(7) Kamat, P. V. *J. Phys. Chem. C* **2008**, *112*, 18737−18753.

(8) Wilker, M. B.; Schnitzenbaumer, K. J.; Dukovic, G. *Isr. J. Chem.* **2012**, *52*, 1002−1015.

(9) Han, Z.; Qiu, F.; Eisenberg, R.; Holland, P. L.; Krauss, T. D. *Science* **2012**, *338*, 1321−1324.

(10) Amirav, L.; Alivisatos, A. P. *J. Phys. Chem. Lett.* **2010**, *1*, 1051−1054.

(11) Jeong, S.; Achermann, M.; Nanda, J.; Ivanov, S.; Klimov, V. I.; Hollingsworth, J. A. *J. Am. Chem. Soc.* **2005**, *127*, 10126−10127.

(12) Aldana, J.; Wang, Y. A.; Peng, X. *J. Am. Chem. Soc.* **2001**, *123*, 8844−8850.

(13) Wuister, S. F.; de Mello Donegá, C.; Meijerink, A. *J. Phys. Chem. B* **2004**, *108*, 17393−17397.

(14) Wu, K.; Chen, Z.; Lv, H.; Zhu, H.; Hill, C. L. *J. Am. Chem. Soc.* **2014**, *136*, 7708−7716.

(15) Kamat, P. V.; Christians, J. A.; Radich, J. G. *Langmuir* **2014**, *30*, 5716−5725.

(16) Abdellah, M.; Marschan, R.; Zidek, K. *J. Phys. Chem. C* **2014**, *118*, 25802−25808.

(17) Marcus, R. A.; Sutin, N. *Biochim. Biophys. Acta, Rev. Bioenerg.* **1985**, *811*, 265−322.

(18) Robel, I.; Kuno, M.; Kamat, P. V. *J. Am. Chem. Soc.* **2007**, *129*, 4136−4137.

(19) Tvrdy, K.; Frantsuzov, P. A.; Kamat, P. V. *Proc. Natl. Acad. Sci. U. S. A.* **2011**, *108*, 29−34.

(20) Huang, J.; Stockwell, D.; Huang, Z.; Mohler, D. L.; Lian, T. *J. Am. Chem. Soc.* **2008**, *130*, 5632−5633.

(21) Boulesbaa, A.; Issac, A.; Stockwell, D.; Huang, Z.; Huang, J.; Guo, J.; Lian, T. *J. Am. Chem. Soc.* **2007**, *129*, 15132−15133.

(22) Zhu, H.; Song, N.; Lian, T. *J. Am. Chem. Soc.* **2010**, *132*, 15038−15045.

(23) Zhu, H.; Yang, Y.; Hyeon-Deuk, K.; Califano, M.; Song, N.; Wang, Y.; Zhang, W.; Prezhdo, O. V.; Lian, T. *Nano Lett.* **2014**, *14*, 1263−1269.

(24) Morris-Cohen, A. J.; Frederick, M. T.; Cass, L. C.; Weiss, E. A. *J. Am. Chem. Soc.* **2011**, *133*, 10146−10154.

(25) Sykora, M.; Petruska, M. A.; Alstrum-Acevedo, J.; Bezel, I.; Meyer, T. J.; Klimov, V. I. *J. Am. Chem. Soc.* **2006**, *128*, 9984−9985.

(26) Huang, J.; Huang, Z.; Jin, S.; Lian, T. *J. Phys. Chem. C* **2008**, *112*, 19734−19738.

(27) Dorokhin, D.; Tomczak, N.; Velders, A. H.; Reinhoudt, D. N.; Vancso, G. J. *J. Phys. Chem. C* **2009**, *113*, 18676−18680.

(28) Malicki, M.; Knowles, K. E.; Weiss, E. A. *Chem. Commun.* **2013**, *49*, 4400−4402.

(29) Tarafder, K.; Surendranath, Y.; Olshansky, J. H.; Alivisatos, A. P.; Wang, L.-W. *J. Am. Chem. Soc.* **2014**, *136*, 5121−5131.

(30) Ding, T. X.; Olshansky, J. H.; Leone, S. R.; Alivisatos, A. P. *J. Am. Chem. Soc.* **2015**, *137*, 2021−2029.

(31) Knowles, K. E.; Peterson, M. D.; McPhail, M. R.; Weiss, E. A. *J. Phys. Chem. C* **2013**, *117*, 10229−10243.

(32) Inkpen, M. S.; Du, S.; Driver, M.; Albrecht, T.; Long, N. J. *Dalton Trans.* **2013**, *42*, 2813−2816.

(33) Tindale, J. J.; Hartlen, K. D.; Alizadeh, A.; Workentin, M. S.; Ragogna, P. J. *Chem. - Eur. J.* **2010**, *16*, 9068−9075.

(34) Zou, C.; Wrighton, M. S. *J. Am. Chem. Soc.* **1990**, *112*, 7578−7584.

(35) Noviandri, I.; Brown, K. N.; Fleming, D. S.; Gulyas, P. T.; Lay, P. A.; Masters, A. F.; Phillips, L. *J. Phys. Chem. B* **1999**, *103*, 6713−6722.

(36) García-Santamaría, F.; Chen, Y.; Vela, J.; Schaller, R. D.; Hollingsworth, J. A.; Klimov, V. I. *Nano Lett.* **2009**, *9*, 3482−3488.

(37) Zhu, H.; Song, N.; Rodríguez-Córdoba, W.; Lian, T. *J. Am. Chem. Soc.* **2012**, *134*, 4250−4257.

(38) Eshet, H.; Grünwald, M.; Rabani, E. *Nano Lett.* **2013**, *13*, 5880−5885.

(39) Hens, Z.; Martins, J. C. *Chem. Mater.* **2013**, *25*, 1211−1221.

(40) Anderson, N. C.; Hendricks, M. P.; Choi, J. J.; Owen, J. S. *J. Am. Chem. Soc.* **2013**, *135*, 18536−18548.

(41) Gomes, R.; Hassinen, A.; Szczygiel, A.; Zhao, Q.; Vantomme, A.; Martins, J. C.; Hens, Z. *J. Phys. Chem. Lett.* **2011**, *2*, 145−152.

(42) Jasieniak, J.; Smith, L.; Embden, J. V.; Mulvaney, P.; Califano, M. *J. Phys. Chem. C* **2009**, *113*, 19468−19474.

(43) Yu, W. W.; Qu, L.; Guo, W.; Peng, X. *Chem. Mater.* **2003**, *15*, 2854−2860.

(44) Chidsey, C. E. *Science* **1991**, *251*, 919−922.

(45) Hyeon-Deuk, K.; Kim, J.; Prezhdo, O. V. *J. Phys. Chem. Lett.* **2015**, *6*, 244−249.

(46) Ekimov, A. I.; Kudryavtsev, I. A.; Efros, L.; Al; Yazeva, T. V.; Hache, F.; Schanne-Klein, M. C.; Rodina, A. V.; Ricard, D.; Flytzanis, C. *J. Opt. Soc. Am. B* **1993**, *10*, 100−107.

(47) Sünkel, K.; Bernhartzeder, S. *J. Organomet. Chem.* **2011**, *696*, 1536−1540.

(48) Menzel, K.; Fisher, E. L.; DiMichele, L.; Frantz, D. E.; Nelson, T. D.; Kress, M. H. *J. Org. Chem.* **2006**, *71*, 2188−2191.

(49) Goeltz, J. C.; Kubiak, C. P. *Organometallics* **2011**, *30*, 3908−3910.

(50) Chen, O.; Zhao, J.; Chauhan, V. P.; Cui, J.; Wong, C.; Harris, D. K.; Wei, H.; Han, H.-S.; Fukumura, D.; Jain, R. K.; Bawendi, M. G. *Nat. Mater.* **2013**, *12*, 445−451.

(51) Wider, G.; Dreier, L. *J. Am. Chem. Soc.* **2006**, *128*, 2571−2576.

(52) Würth, C.; Grabolle, M.; Pauli, J.; Spieles, M.; Resch-Genger, U. *Anal. Chem.* **2011**, *83*, 3431−3439.